Petroleum Science 23 (2026) 3213–3227

Contents lists available at ScienceDirect

Petroleum Science

journal homepage: www.keaipublishing.com/en/journals/petroleum-science

Original Paper

Beyond spatial averaging: Modeling DAS seismic responses with optical system effects

Yi Yao [a,b], Yi-Bo Wang [a,b,*]

[a] Key Laboratory of Deep Petroleum Intelligent Exploration and Development, Institute of Geology and Geophysics, Chinese Academy of Sciences, Beijing, 100029, China

[b] College of Earth and Planetary Sciences, University of Chinese Academy of Sciences, Beijing, 100049, China

A R T I C L E I N F O

Article history:
Received 6 September 2025
Received in revised form
30 November 2025
Accepted 5 February 2026
Available online 14 February 2026

Edited by Meng-Jiao Zhou

Keywords:
Distributed acoustic sensing
Numerical simulation
Optical system
Seismic response

A B S T R A C T

Distributed acoustic sensing (DAS) utilizes standard optical fibers as continuous distributed seismic sensors, enabling the acquisition of subsurface vibration information with high spatial sampling density and long-distance coverage. Existing numerical simulation methods for DAS data typically rely on solving elastic wave equations and are implemented through simplified processes such as axial projection along the fiber and spatial averaging. However, this approach neglects the influence of optical systems on DAS responses, including Rayleigh scattering, coherent detection, and signal demodulation, making it difficult to comprehensively reflect the response characteristics of actual DAS systems. To address this deficiency, this study proposes a DAS seismic response numerical simulation framework that integrates physical processes. We introduce Rayleigh scattering modeling and demodulation mechanisms for coherent OTDR (optical time domain reflectometry) in the simulation, and systematically consider key parameters including pulse width, gauge length, polarization fading, laser frequency drift, phase noise, and detector noise. Simulation results demonstrate that, under ideal noise-free conditions, the new model yields result highly consistent with those of the traditional spatial averaging model, validating its accuracy. In the presence of environmental noise, the proposed method produces smoother responses compared to traditional approaches, indicating a certain denoising advantage. When optical system noise is introduced, the physics-based simulation can reproduce complex phenomena observed in actual measurements, such as phase fading noise and frequency drift noise. These findings underscore the necessity and effectiveness of a physical model in capturing the true behavior of DAS systems. The proposed simulation framework provides a critical foundation for optimizing DAS system design, enhancing signal-to-noise ratios, and improving DAS data inversion. It holds significant guiding implications for the future application of DAS in seismic monitoring.

1. Introduction

Seismic data are critical geophysical resources for studying large-scale subsurface structures and characterizing subsurface medium properties with high resolution. Major advances in seismology have primarily stemmed from innovations in observational techniques (Shearer, 2009). Traditionally, seismic observations have relied on velocity-type seismometers based on Faraday's law of electromagnetic induction, commonly referred to as seismic sensors or seismographs. These sensors, typically consisting of a magnet-spring system coupled with a coil, precisely measure the three-component particle velocity induced by seismic waves.

In recent years, optic sensing technology has developed rapidly in the field of geophysics, offering new technical avenues for seismic observation (Wang et al., 2022a). Fiber optic sensors exploit the sensitivity of light propagating in optical fibers to external physical quantities, such as strain, temperature, and pressure, by detecting changes in light intensity, phase, polarization state, or wavelength to achieve precise measurement of the

* Corresponding author.
E-mail address: wangyibo@mail.iggcas.ac.cn (Y.-B. Wang).

Peer review under the responsibility of China University of Petroleum (Beijing).

https://doi.org/10.1016/j.petsci.2026.02.007
1995-8226/

targeted parameters. Depending on the sensing principle, fiber optic sensing technologies can be classified into point-based and distributed systems. Point-based fiber optic sensors mainly include Fiber Bragg Grating (FBG) sensors and interferometer-based fiber optic sensors. FBG sensors measure strain or temperature changes by monitoring the Bragg wavelength shift of periodic refractive index modulations in the fiber and have long been widely applied in structural health monitoring (Kok et al., 2024). Interferometer-based fiber sensors, on the other hand, detect external disturbances through phase differences of coherent light in different optical paths, offering extremely high sensitivity, and have been successfully applied in geophysical exploration (Liu et al., 2020). However, these point-based sensors are inherently discrete measurement systems, requiring the pre-fabrication of multiple sensing points along the fiber or the construction of complex interferometric paths, which limits their application in large-scale continuous monitoring.

Compared with traditional point-based sensors, distributed fiber optic sensing (DFOS) technology enables continuous spatial measurement along the fiber, providing high-resolution environmental information over long distances. DFOS mainly includes distributed acoustic sensing (DAS), distributed temperature sensing (DTS), and distributed strain/stress sensing (DSS) (Wang et al., 2022b). Its basic principle relies on the scattering characteristics of light in optical fibers, such as Rayleigh, Brillouin, or Raman scattering, allowing continuous acquisition of acoustic, temperature, or strain information along the fiber by monitoring changes in the optical signal. Compared to conventional sensors, DFOS offers significant advantages: it can cover large areas without installing separate sensors at each measurement point; the optical fiber itself is corrosion-resistant, immune to electromagnetic interference, and adaptable to complex environments; and it can achieve high spatial resolution with long-term continuous monitoring (Spikes et al., 2019; Mateeva et al., 2014). In particular, distributed acoustic sensing is capable of high-frequency acquisition, which has drawn widespread attention and rapid development in geophysics in recent years, laying a technical foundation for seismic monitoring and related applications.

DAS technology has demonstrated broad applications across multiple fields in recent years and continues to develop rapidly. Initially used for qualitative detection in security monitoring applications such as perimeter intrusion, oil and gas pipeline leakage, power transmission lines, and railway vibrations, DAS has now expanded to become a high-precision quantitative observation tool in numerous seismological scenarios, including: borehole vertical seismic profiling (VSP) (Lellouch et al., 2021), downhole microseismic monitoring (Lellouch et al., 2020; Grandi et al., 2017; Cole and Karrenbach, 2019; Molteni et al., 2017), hydraulic fracturing-induced seismic monitoring (Jin and Roy, 2017; Jin et al., 2019b; Ichikawa et al., 2020), urban microseismic detection (Ajo-Franklin et al., 2019; Lindsey et al., 2020; Jakkampudi et al., 2020), and deep structural imaging (Nishimura et al., 2021; Lior et al., 2021; Walter et al., 2020). Thus, DAS is becoming an important tool in the field of seismic monitoring.

Furthermore, DAS can be integrated with other optical sensing devices to build multi-parameter monitoring systems, further extending the applications of fiber optic sensing in geophysics. For example, combining DAS with DTS technology allows simultaneous acquisition of strain and temperature distributions along the fiber, which is valuable for production profile monitoring in oil and gas wells (Jin et al., 2019a). In the field of submarine seismic observation, researchers have integrated DAS with fiber-optic hydrophone arrays to achieve multi-dimensional collaborative observation of seabed seismic wavefields and ocean acoustic signals (Matsumoto et al., 2021). This multi-technology integrated monitoring schemes fully leverage the strengths of different sensor types, providing richer and more reliable data support for the study of complex geophysical problems.

However, despite significant progress in seismic monitoring applications, fully exploiting the data value of DAS still depends on a thorough understanding of wavefield response mechanisms. DAS observations are influenced by multiple factors including seismic wave types, optical fiber medium properties, coupling conditions, and array geometry. Therefore, conducting joint numerical simulations of wave propagation and DAS system response is crucial for correctly interpreting DAS data. Current mainstream DAS numerical simulation strategies typically employ a simplified workflow of "elastic wave equation solving + fiber axial projection + spatial sliding averaging" to approximate DAS signals. The above simplified approach is convenient to implement and computationally efficient, and has been widely applied in studies such as synthetic seismic data generation, comparison of DAS and traditional geophone responses, and optimization of fiber deployment geometry (Vera Rodriguez and Wuestefeld, 2020; Eaid, 2022; Zhang et al., 2024). While this method has reference value to some extent, it also has obvious limitations: it only considers mechanical strain caused by seismic waves, ignoring the effects of a series of optical processes involved in DAS as an optical sensing system, including Rayleigh scattering, coherent detection, photoelectric conversion, and signal demodulation on observations. In other words, existing simplified models implicitly assume complete linearity and ideal superposition, incorporating only the gauge length as a system parameter while excluding others (e.g., pulse width, laser phase noise). These idealized assumptions reduce simulation complexity but deviate significantly from the actual physical behavior of DAS systems.

Given the critical role of DAS in seismology, there is an urgent need to develop more physically realistic numerical simulation methods. Only by accurately simulating the response characteristics of DAS systems can we gain deeper insights into the physical nature of observational data and provide forward modeling support for optimizing system design, enhancing signal-to-noise ratios, and improving data inversion reliability. This study aims to overcome the oversimplification limitations of traditional DAS simulations by proposing a novel simulation framework that integrates the optical link demodulation mechanism. Building on elastic wavefield simulations, we incorporate Rayleigh scattering modeling and coherent detection principles, conducting perturbation analyses on key system parameters such as pulse width, polarization fading, laser frequency drift, phase noise, and detector noise to explore their mechanisms and impacts on DAS signals. Through this more realistic simulation framework, we aim to provide reliable theoretical guidance for optimizing DAS observation systems, improving signal-to-noise ratios, and enhancing data interpretation.

2. Method

2.1. Review of existing methods

A systematic review of the literature on DAS applications in seismology over the past five years reveals that current mainstream simulation approaches follow highly consistent technical approaches (Lecoulant et al., 2023; Yao et al., 2023). The vast majority of studies adhere to the following workflow: First, elastic wave equations are solved using numerical simulation methods such as analytical solutions, finite difference, or spectral element methods to obtain three-dimensional spatiotemporal displacement or strain fields in the target area. Second, according to the actual deployment path of the optical fiber, the wavefield is projected along the fiber axis through tensor projection, retaining only the axial strain components along the fiber direction to match the DAS system's sensitive response to axial micro-strain. Third, for each measurement point along the fiber, the projected axial strain values are window-averaged within a given gauge length range to simulate the spatial integration response generated by the DAS system over that fiber segment. The above workflow can be simplified and represented by the following mathematical model:

$$\varepsilon_{\mathrm{DAS}}(x,t) \approx \frac{1}{L_{\mathrm{G}}}\int_{x-\frac{L_{\mathrm{G}}}{2}}^{x+\frac{L_{\mathrm{G}}}{2}} \varepsilon(x,t)\mathrm{d}x \tag{1}$$

where $\varepsilon_{\mathrm{DAS}}(x,t)$ represents the simulated DAS strain response, L_{G} is the gauge length, and $\varepsilon(x,t)$ is the strain field along the fiber direction. The above model is simple, clear, and easy to implement, and has therefore been widely adopted in studies such as synthetic seismic data generation, deployment geometry sensitivity analysis, and source mechanism comparison.

However, this highly simplified modeling approach implicitly incorporates several critical idealized assumptions: for example, it assumes that the system response is strictly linear and that signal superposition satisfies the ideal linear summation principle; except for the gauge length as a spatial averaging parameter, other system parameters (such as optical pulse width, laser phase noise, etc.) are not included in the model considerations. While simplified assumptions reduce simulation complexity, they are far from the actual physical behavior of real DAS systems.

In summary, this traditional strategy of "strain projection + spatial averaging" is essentially only a mathematical approximation rather than physical modeling, and therefore has several important limitations: (1) it cannot reproduce the true response characteristics of DAS systems; (2) it cannot predict the effects of various actual noise sources on signals; (3) it cannot provide reliable forward modeling basis for system design and optimization, with its applicability and physical interpretability being significantly limited.

2.2. Coherent-OTDR numerical model

In recent years, some studies have begun attempting more physically-based simulation modeling of DAS systems based on the principle of optical fiber Rayleigh backscattering, particularly for the most widely applied coherent-type OTDR (Optical Time-Domain Reflectometry) systems. Liokumovich et al. (2015) established a numerical simulation model for coherent OTDR systems; subsequently, Zhao et al. (2024) developed high-fidelity coherent OTDR simulation methods considering the effects of various interferences and noise sources.

The basic working principle of coherent OTDR systems is shown in Fig. 1. Light from a narrow-linewidth continuous-wave laser is split into two paths through an optical coupler (OC): one path is modulated into short pulses through an acousto-optic modulator (AOM) and amplified by an erbium-doped fiber amplifier (EDFA) before being injected into the single-mode fiber (SMF) under test through a circulator (CIR), exciting Rayleigh backscatter (RBS) within the fiber; the other branch serves as local reference light and directly enters the reference arm. The backscattered signals from the fiber under test are extracted through the CIR and combined with the reference light at the optical coupler, generating optical beat frequency electrical signals through a balanced photodetector (BPD). Finally, after filtering through a bandpass filter (BPF), sampling by a data acquisition system (DAQ), and demodulation processing within a computer, vibration strain information along the fiber can be extracted from the BPD signals.

To numerically simulate the above process, we first need to model Rayleigh scattering within the optical fiber. A discrete scattering model (Fig. 2) is typically adopted as the numerical simulation basis for Rayleigh scattered light: the optical fiber is discretized into equal-length small segments, with the center point of each segment selected as a scattering element. When the probe pulse is injected into the fiber, the Rayleigh backscattered light generated by M scattering points superimposes to form the total backward signal. The backscattered complex amplitude generated by the k-th scattering point can be expressed as:

$$E_{\mathrm{R}}(k)=\begin{cases} E_0\sum\limits_{k-M}^{k} r_k \exp(-2\alpha k\Delta L)\exp\{j(2\pi(f_0+f_{\mathrm{AOM}})\cdot t_k+\varphi_0)\}, k>M \\ E_0\sum\limits_{1}^{k} r_k \exp(-2\alpha k\Delta L)\exp\{j(2\pi(f_0+f_{\mathrm{AOM}})\cdot t_k+\varphi_0)\}, k\le M \end{cases} \tag{2}$$

$$t_k = t_{k-1} + \frac{2n_k}{c}\Delta L + \frac{2n_k'}{c}(D_k - D_{k-1}) \tag{3}$$

where E_0 represents the amplitude of the pulsed light, r_k is the scattering coefficient of the scattering point, α is the attenuation coefficient of the sensing fiber, and j is the imaginary unit. f_0 is the center frequency of the laser, f_{AOM} is the frequency offset generated by the AOM, and φ_0 is the initial phase of the pulsed light, which is a constant under ideal conditions. The medium displacement at the k-th point is denoted as D_k. In our simulation, we assume complete coupling between the fiber and the medium, i.e., the particle displacement of the medium is equivalent to the displacement at the corresponding position of the fiber.

In practice, the phase variation of the backscattered light induced by external vibrations consists of two aspects: the change in the geometrical length of the fiber, and the change in the refractive index of the material. For the silica medium of the optical fiber, the sensitivity coefficient of the refractive index to displacement variations is expressed as follows (Masoudi and Newson, 2017):

$$n_k' = n_k\left(1 - 0.5n_k^2[(1-\mu)p_{12} - \mu p_{11}]\right) \tag{4}$$

Let

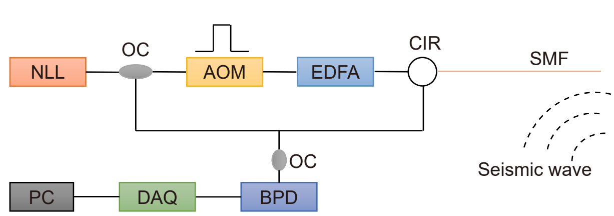

Fig. 1. Schematic diagram of a coherent φ-OTDR system.

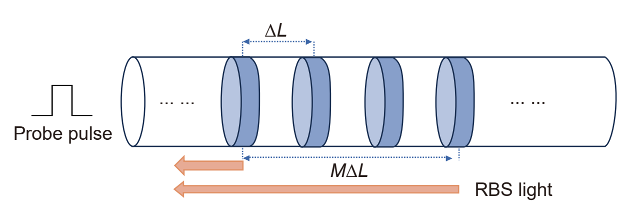

Fig. 2. Rayleigh discrete scattering model.

$$\zeta = \left(1 - 0.5n_k^2[(1-\mu)p_{12} - \mu p_{11}]\right) \tag{5}$$

and define the strain as

$$\varepsilon_k = (D_k - D_{k-1}) / \Delta L \tag{6}$$

thus Eq. (3) can be rewritten as

$$t_k = t_{k-1} + \frac{2n_k}{c}\Delta L + \frac{2\zeta n_k}{c}\varepsilon_k \Delta L \tag{7}$$

The last term in Eq. (7) represents the optical path delay induced by seismic vibrations. By multiplying it with the optical frequency, the additional phase delay caused by the disturbance can be obtained. Therefore, the approximate relation between strain and phase variation can be written as:

$$\varphi_k = \varphi_{k-1} + \frac{4\pi\zeta n f_0}{c}\varepsilon_k \Delta L \tag{8}$$

As evident from the equations, the phase demonstrates a cumulative effect along the fiber (Sha et al., 2017). The backscattered Rayleigh signal derived above can be expressed mathematically, while on the other hand the contribution of the local reference light must also be considered. The reference light can be expressed as:

$$E_{\mathrm{L}}(k) = E_{\mathrm{L0}} \exp\left(j(2\pi f_0 t_k)\right) \tag{9}$$

where E_{L0} denotes the amplitude of the reference light. When the backscattered light $E_{\mathrm{R}}(k)$ and the reference light $E_{\mathrm{L}}(k)$ are recombined at the optical coupler and subsequently received by BPD, the output beat signal can be expressed as:

$$I(k) = \mathrm{real}(E_{\mathrm{R}}(k)\cdot \mathrm{conj}(E_{\mathrm{L}}(k))) = A\cos(2\pi f_{\mathrm{AOM}} t_k + \varphi_k) \tag{10}$$

Extracting the distributed vibration-induced phase along the fiber is the key step of DAS demodulation. At present, the standard method is quadrature demodulation (or arctangent method) (Li et al., 2023; Lu et al., 2010). Specifically, the beat signal in Eq. (10) is respectively multiplied by orthogonal carriers $\cos(2\pi f_{\mathrm{AOM}} t_k)$ and $\sin(2\pi f_{\mathrm{AOM}} t_k)$, and then passed through a low-pass filter to obtain two quadrature signals:

$$I(k) = A/2 \cos(\varphi_k) \tag{11}$$

$$Q(k) = -A/2 \sin(\varphi_k) \tag{12}$$

Dividing Eq. (12) by Eq. (11) and applying the arctangent operation yields the recovered phase value:

$$\varphi_k = -\arctan\left(\frac{Q(k)}{I(k)}\right) \tag{13}$$

It should be noted that the above φ_k actually represents the cumulative phase perturbation from the fiber input to the k-th point (Eq. (6)), which includes the phase variations of all preceding scattering points. However, what we ideally expect is the local phase variation $\Delta\varphi$ at the k-th point itself. According to the principle of phase difference between adjacent scattering points, the actual localized phase variation at the k-th point can be expressed as:

$$\Delta\varphi = \varphi_{k+1} - \varphi_{k-1} \tag{14}$$

Nevertheless, due to the finite spatial pulse width, the scattered signals from neighboring points overlap partially in time, making them difficult to completely separate. To address this, the concept of gauge length is introduced: a spatial interval containing several scattering points is chosen as the phase-difference spacing. This gauge length must be at least greater than the pulse width to ensure that the backscattered signals from adjacent intervals remain independent. Accordingly, Eq. (14) can be extended to represent the phase difference over a gauge length:

$$\Delta\varphi_k = \varphi_{k+N/2} - \varphi_{k-N/2} \tag{15}$$

where N corresponds to the number of scattering points contained within the gauge length. By applying this differencing scheme, the phase variation over each gauge interval can be obtained. Using the previously described strain–phase relation (Eq. (8)), the phase difference can then be converted into the axial strain response:

$$\Delta\varphi_k = \frac{4\pi\zeta n f_0}{c}\sum_{k-N/2}^{k+N/2}\varepsilon_k \Delta L = \frac{4\pi\zeta n f_0 L_G}{c}\varepsilon_k \tag{16}$$

That is,

$$\varepsilon_k = \frac{c}{4\pi\zeta n f_0 L_G}\Delta\varphi_k \tag{17}$$

Eq. (17) provides the physically modeled simulated strain measurement at the k-th point of a DAS system. Compared with the conventional numerical averaging approach, this result is derived from a physical simulation of Rayleigh backscattering, optical detection, and signal demodulation, thereby yielding outcomes that more closely represent actual DAS observations.

2.3. Model parameters

As shown by the simulation results of coherent φ-OTDR, numerical modeling of DAS involves multiple system parameters. To better approximate real-world conditions, the following key factors are considered in our modeling framework:

1) Refractive index fluctuations: In practice, optical fibers exhibit slight refractive index variations along their length due to manufacturing imperfections. To reflect this characteristic, we introduce random perturbations to the baseline refractive index in our model. This study employs a light-averaged refractive index of $n = 1.5$, with small random variations (10^{-6} magnitude) added to simulate non-uniformity, which can be characterized by a uniform distribution (Liokumovich et al., 2015).
2) Scattering coefficient randomness: The Rayleigh scattering strength within optical fibers is non-uniform and follows random fluctuations. During simulation, the scattering coefficient for each scattering point is sampled from a Rayleigh distribution (Liokumovich et al., 2015) to better reflect the actual distribution characteristics of scattering points.
3) Polarization angle: In DAS systems, polarization variations between signal and reference light significantly affect interference strength. Due to environmental perturbations, the polarization of scattered light within the fiber can be considered a randomly varying quantity. If θ_k represents the polarization angle of scattered light relative to the reference light at the k-th point, the backscattered signal requires additional

consideration of polarization-induced amplitude modulation (Ren et al., 2016). For simplicity, this can be incorporated into the model by modifying Eq. (2) to include the polarization term:

$$E_R(k) = \begin{cases} E_0 \sum_{k-M}^{k} r_k \exp(-2\alpha k \Delta L) \exp\{j(2\pi(f_0 + f_{AOM}) \cdot t_k + \varphi_0)\} \cos(\theta_k), k > M \\ E_0 \sum_{1}^{k} r_k \exp(-2\alpha k \Delta L) \exp\{j(2\pi(f_0 + f_{AOM}) \cdot t_k + \varphi_0)\} \cos(\theta_k), k \le M \end{cases} \tag{18}$$

4) Laser frequency drift: The long-term stability of laser frequency directly affects the phase baseline of detection. Under ideal conditions, the detection light frequency remains constant, but in practice, environmental temperature changes and other factors cause slow frequency drift in the laser. Additionally, mechanical vibrations can produce instantaneous frequency fluctuations (Zhong et al., 2021). To simulate these phenomena, we introduce a time-varying frequency drift term into the reference light Eq. (9) modifying it as:

$$E_L(k) = E_{L0} \exp(j(2\pi(f_0 + \Delta f) t_k)) \tag{19}$$

where Δf is the frequency drift term describing random temporal variations in frequency (such as setting a constant drift rate or random drift process). Correspondingly, cumulative phase shifts appear in beat frequency signals, and this modification enables simulation of frequency drift noise effects on DAS signals.

5) Laser phase noise: Practical lasers exhibit inherent phase noise, meaning the phase undergoes random fluctuations that directly affect the phase stability of beat frequency signals. To account for this factor, we add a random noise term to the reference light phase (typically modeled as a zero-mean random process) (Zhang et al., 2020). Correspondingly, Eq. (9) can be modified as:

$$E_L(k) = E_{L0} \exp(j(2\pi f_0 t_k + \varphi(t_k))) \tag{20}$$

6) Detector noise (BPD noise): Balanced photodetectors introduce electronic noise during the photoelectric conversion process, particularly under weak backscattered signal conditions where detector baseline noise may mask useful signal portions. We simulate BPD output noise by adding a broadband noise term to the beat frequency signal Eq. (10):

$$I(k) = A\cos(2\pi f_{AOM} t_k + \varphi_k) + N(k) \tag{21}$$

where $N(k)$ represents the detector noise term. Related research shows that BPD output noise statistically approximates a Gaussian distribution (Kim et al., 2009). By introducing this term, we can evaluate the impact of instrument noise on DAS signal quality.

7) Pulse width and gauge length: Pulse width and gauge length are important design parameters of DAS systems that directly affect spatial resolution and signal-to-noise characteristics. It should be noted that for computational and explanatory convenience, although pulse width actually represents the temporal duration of the pulse, we express it in terms of distance throughout the following text—that is, the length that light travels during this time period. In our physical model implementation, pulse width is primarily controlled by parameter M—representing the number of scattering points simultaneously participating in coherent superposition when each pulse is incident (proportional to the spatial length corresponding to the pulse width); gauge length is controlled by parameter N—representing the interval number of scattering points used for phase differencing. By selecting different values of M and N, we can simulate DAS system responses under different pulse durations and gauge length settings, thereby analyzing the effects of pulse width and gauge length on signals. In specific implementation, it should be ensured that the length corresponding to N is not smaller than the pulse length corresponding to M, to satisfy the basic requirement that gauge length exceeds pulse width.

2.4. Physical model DAS simulation framework

Based on the modeling of the above components, we have constructed a physical model-based DAS numerical simulation workflow (Fig. 3(b)). To highlight the characteristics of the new approach, Fig. 3(a) provides a comparison with the traditional spatial averaging simplified model workflow. It can be observed that the simplified model only requires elastic wavefield and gauge length parameters to generate DAS signals, with the option to superimpose external environmental noise, resulting in low computational cost and having certain application value in rapid evaluation of gauge length selection. However, due to the assumption of idealized optical links, the simplified model cannot reproduce various optical noise and nonlinear effects in actual DAS systems.

In contrast, the physics-based simulation method considers optical system parameters including light scattering, coherent superposition, polarization angle, frequency drift, phase noise, and detector noise, enabling the generation of high-fidelity DAS synthetic data under different operating conditions. This approach facilitates in-depth research into DAS system response performance and performance limits under complex conditions.

3. Numerical simulation results

3.1. Seismic scenario configuration

We selected a DAS monitoring scenario that closely resembles real-world applications to conduct the numerical simulation. The observation system is based on a monitoring well at a shale gas hydraulic fracturing site, providing a realistic downhole configuration for DAS deployment. A seismic source is placed in the target zone near the perforation clusters (indicated by the red pentagram

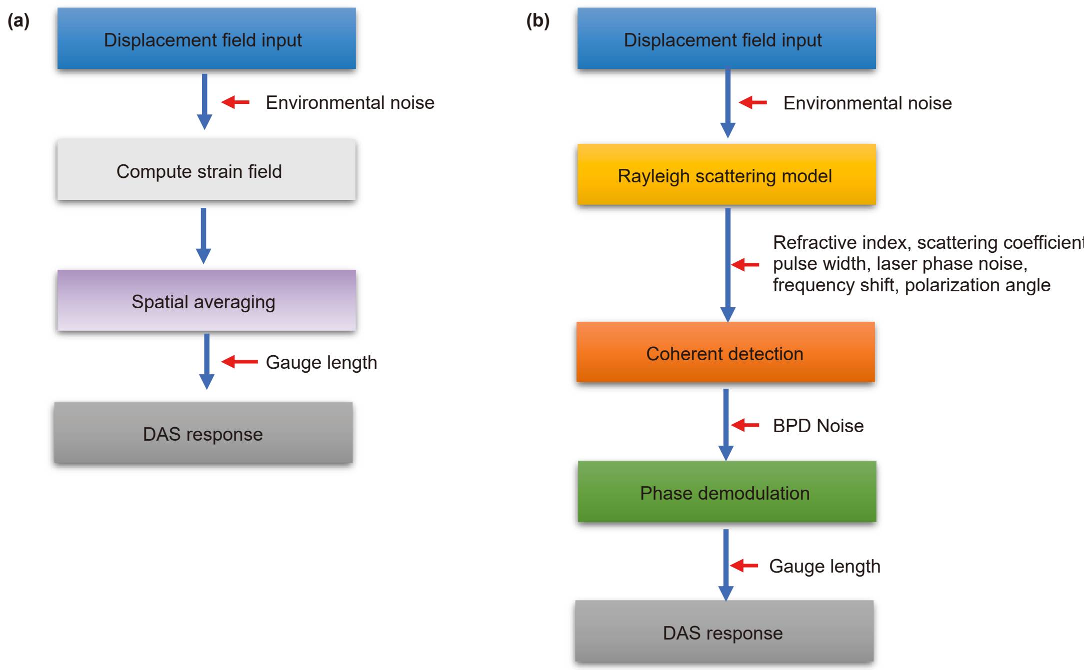

Fig. 3. Comparison of DAS numerical simulation workflows based on **(a)** spatial averaging simplification versus **(b)** physical modeling. The displacement field inputs are both projected along the fiber direction. Red arrows indicate noise sources or system parameters that can be injected at corresponding stages to generate multi-scenario, high-fidelity DAS synthetic data.

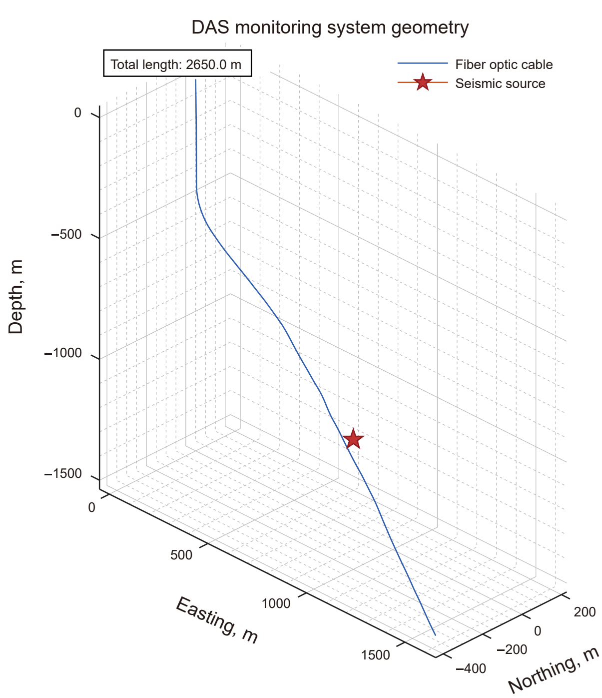

Fig. 4. Observation system in the DAS numerical simulation experiment. The source can radiate toward the curved optical fiber with complex deployment paths. The red pentagram marks the source location. The total fiber length is approximately 2650 m, and this configuration is used to simulate DAS responses under shale gas fracturing scenarios.

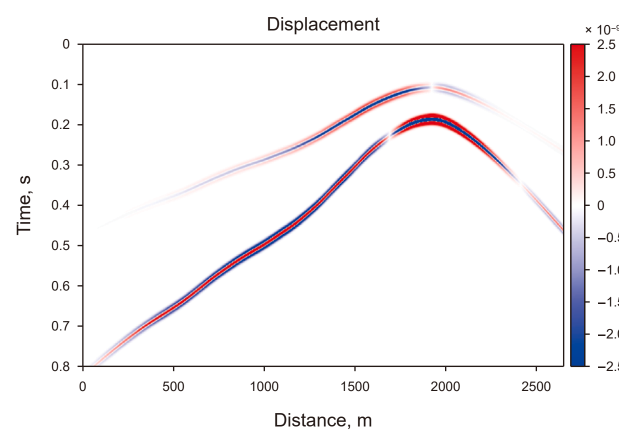

Fig. 5. Distribution of the displacement field after axial projection of the optical fiber. The figure illustrates the axial displacement response along the fiber induced by the seismic source, which serves as the input for subsequent DAS signal calculations. The color scale denotes the displacement amplitude in different directions, with red and blue corresponding to positive and negative polarities, respectively.

in Fig. 4) to simulate the typical microseismic response during fracturing operations. The source time function is a Ricker wavelet with a dominant frequency of 50 Hz, and the source mechanism is configured as a pure double-couple rupture.

For the subsurface medium model, we assume that layer is a homogeneous and isotropic elastic medium. The P-wave velocity is set to 3000 m/s, the S-wave velocity to 1731 m/s, with a spatial grid spacing of 0.1 m and a time step of 1 ms. The grid size is 801 $\times$ 26,500. Because this model represents a simplified, semi-infinite half-space, the three-component displacement field at each fiber channel location can be computed directly using analytical formulation.

After obtaining the three-component elastic wavefield, we incorporate the actual measurement physics of DAS instruments. In real downhole installations, optical fibers are typically well-coupled to intact rock formations, and their path orientation remains stable along the well trajectory. Therefore, we project the

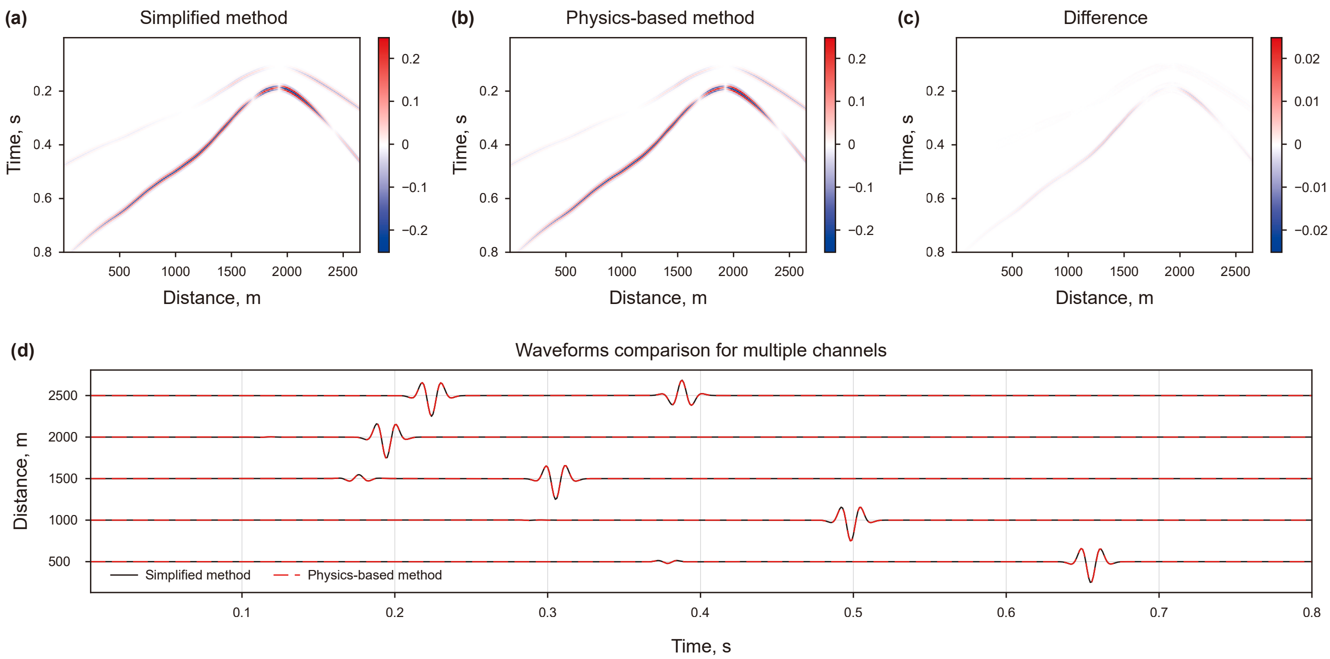

Fig. 6. Comparison of DAS responses under ideal noise-free conditions. **(a)** and **(b)** show the spatiotemporal DAS sections simulated using the simplified model and the physics-based model, respectively. **(c)** presents the difference between the two results, and **(d)** compares the waveforms of multiple channels.

displacement vector onto the local axial direction of the fiber to obtain the axial displacement to which DAS is sensitive:

$$u_l = R_{lx}u_x + R_{ly}u_y + R_{lz}u_z \tag{22}$$

where l denotes the local axial direction of the fiber, u_l is the projected fiber-axial displacement, $[u_x, u_y, u_z]$ are the three-component displacements, and R_{lm} represents the cosine of the angle between the fiber axis l and the corresponding coordinate axis m.

This projection step is essential because DAS instruments do not respond to full vector displacement; instead, they are sensitive only to axial strain or the axial gradient of displacement along the fiber. Therefore, Fig. 5 presents the physically meaningful axial displacement distribution, which serves as the mechanical input for the subsequent optical-domain simulation. This figure intuitively illustrates how seismic disturbances propagate along the fiber and represents the critical linkage between elastic wave

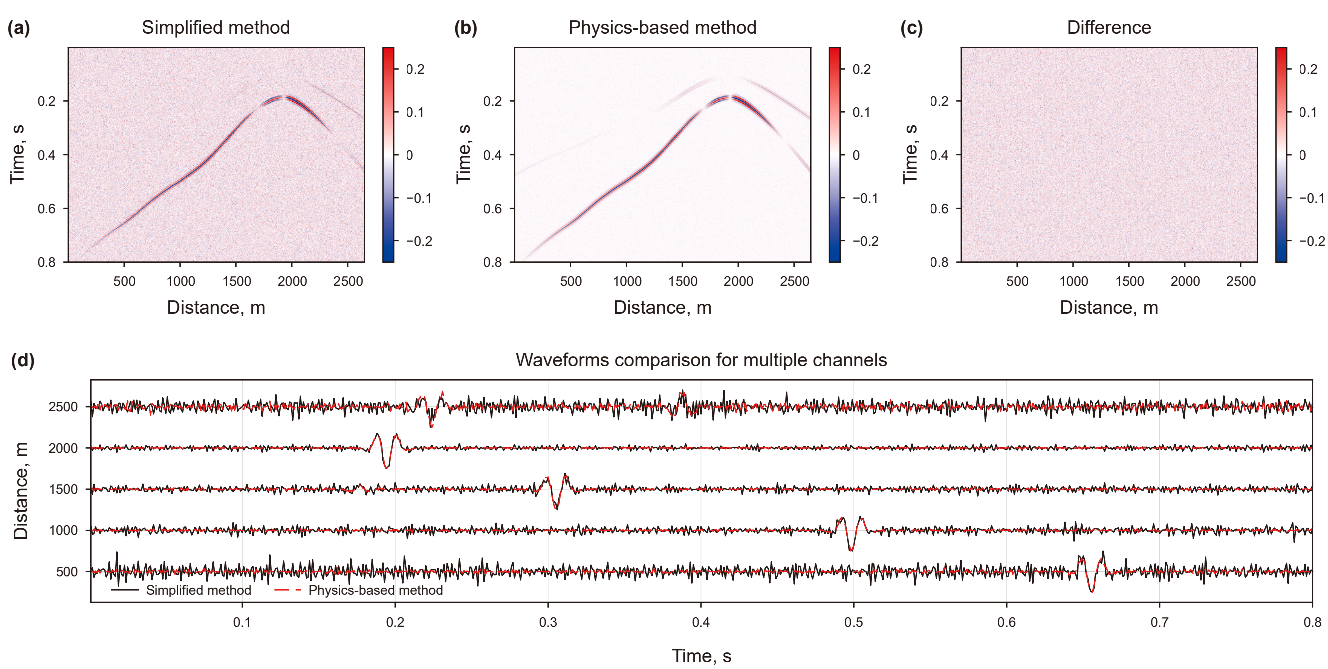

Fig. 7. Comparison of DAS responses under noisy conditions. **(a)** and **(b)** show the spatiotemporal DAS sections simulated using the simplified model and the physics-based model, respectively. **(c)** presents the difference between the two results, and **(d)** compares the waveforms of multiple channels.

modeling and optical demodulation, forming the foundation for synthetic DAS signal generation.

3.2. Model validation and comparison

We first designed an idealized experiment to compare the two modeling approaches. In this experiment, for the full-physics DAS responses simulation, all system parameters were simplified to their most basic state in order to eliminate uncertainties. Specifically, the refractive index was set as a constant with no random perturbations; scattering coefficients were assigned uniform values to remove the effect of coherent fading; the pulse width was set sufficiently narrow to prevent overlap of neighboring scattering signals (equivalent to ideal spatial resolution); and all noise terms—including polarization noise, frequency drift, phase noise, and detector noise—were set to zero, thereby simulating a perfectly noise-free environment. Under these conditions, we performed DAS strain-response simulations of the same well seismic wavefield using both the conventional spatial-averaging model and the full-physics optical model. As shown in Fig. 6, the spatiotemporal DAS sections obtained by the two methods are nearly identical, with individual traces closely overlapping. The differences are negligible, indicating that under ideal, disturbance-free conditions, the simplified model and the full-physics model yield consistent results.

Next, to evaluate the adaptability of the physical model under more complex conditions, we superimposed random noise of a certain amplitude onto the ideal displacement field (representing environmental or medium-related disturbances), and again simulated the DAS responses using both approaches. Fig. 7 shows the comparison of DAS strain records under noisy conditions. Interestingly, despite the added noise, the DAS responses simulated by the physical model is smoother and more stable than that from the simplified model, with significantly reduced high-frequency fluctuations, demonstrating a notable “denoising” effect. This difference arises because the physical model inherently incorporates coherent accumulation and filtering processes within the optical detection chain, which suppress high-frequency random noise. In contrast, the simplified model merely superimposes noise on the wavefield before spatial averaging, without reflecting such smoothing effects. Consequently, the full-physics model produces a more stable output in noisy environments.

To quantitatively evaluate the noise suppression capability of the proposed forward modeling method, we calculated the SNR of DAS responses processed by both the conventional spatial averaging approach and our proposed method. The SNR was computed using the ratio of signal power to background noise power. Table 1 provides a quantitative comparison of the noise-suppression performance between the traditional method and the proposed optical-demodulation-based forward modeling across three representative scenarios. For all cases, the conventional method exhibits a pronounced degradation in SNR after spatial differentiation, decreasing from 9.45 dB → 1.12 dB → 0.25 dB as the noise level increases. This strong sensitivity to noise is expected, as taking spatial derivatives inherently amplifies high-frequency noise components added at the displacement level, resulting in severely distorted strain or strain-rate responses. In contrast, the proposed method consistently achieves much higher SNRs of 20.00 dB → 6.94 dB → 2.92 dB under the same conditions. Although SNR naturally decreases as noise becomes stronger, the reduction is significantly less severe compared with the traditional method. Overall, the numerical results show that the proposed approach provides an SNR improvement of roughly 10–15 dB over the traditional method across different noise levels.

Table 1
Quantitative comparison of SNR (dB) between the traditional method and the proposed method under different noise levels.

Methods	SNR, dB		
Traditional method	9.45	1.12	0.25
Proposed method	20.00	6.94	2.92

3.3. DAS responses to fading noise

In DAS systems, fading noise primarily arises from two mechanisms: coherent fading and polarization fading. Coherent fading originates from constructive and destructive interference among echoes from multiple scattering points, with its statistical characteristics determined by random fluctuations in scattering coefficients and perturbations in the refractive index distribution. Polarization fading, on the other hand, results from random mismatches between the polarization states of the signal and reference light, leading to additional intensity fluctuations at the detection end. In our simulations, these two types of fading can be independently reproduced by adjusting specific parameters. Coherent fading is modeled through the randomness of scattering coefficients, refractive index perturbations, and phase noise, while polarization fading is introduced by randomizing the polarization angle. Fig. 8 presents a comparison of DAS records under conditions of pure coherent fading (Fig. 8(a)) and pure polarization fading (Fig. 8(b)).

The results indicate that, although the physical origins of the two fading types differ, their manifestations in DAS records are strikingly similar. Both exhibit spurious spiky fluctuations and abrupt phase jumps within seismic signal bands, while some fixed spatial positions show persistently low amplitudes, forming vertical dark stripes along depth. These effects become more pronounced when instrumental noise is included. Such amplitude collapses directly reduce the effective signal-to-noise ratio of phase demodulation, thereby limiting the system's capability to detect weak vibration events.

3.4. DAS responses to frequency drift noise

Frequency drift noise arises from temporal variations in the laser source frequency, leading to signal instability. In a coherent OTDR system, even extremely small frequency drifts can accumulate over time and cause a shift in the phase reference of the backscattered light, thereby degrading demodulation accuracy. Two common forms of frequency noise are typically considered: (i) slow drift, such as gradual frequency deviations induced by temperature fluctuations of the laser, and (ii) transient jumps, such as brief frequency spikes triggered by mechanical shocks.

In our simulations, both types of noise were modeled by introducing different forms of $\Delta f(t)$ into the reference light frequency, and their effects on DAS signals were analyzed. Fig. 9 shows the simulated results: Fig. 9(a) corresponds to continuous linear frequency drift. To magnify the effect, the drift rate was set to -50 kHz/s in the simulation. The results indicate that with increasing time, the vibration signals in DAS records accumulate errors along the propagation distance. When the drift rate is sufficiently small, this effect may not be noticeable.

Fig. 9(b) corresponds to a transient frequency jump, where the laser frequency was instantaneously increased at a specific moment and then quickly restored to zero-drift. This results in simultaneous, intense abnormal vibrations across almost all fiber channels, appearing as a distinct horizontal stripe in the record. Because such noise occurs synchronously across all channels with identical amplitude and phase shifts, it is often referred to as common-mode

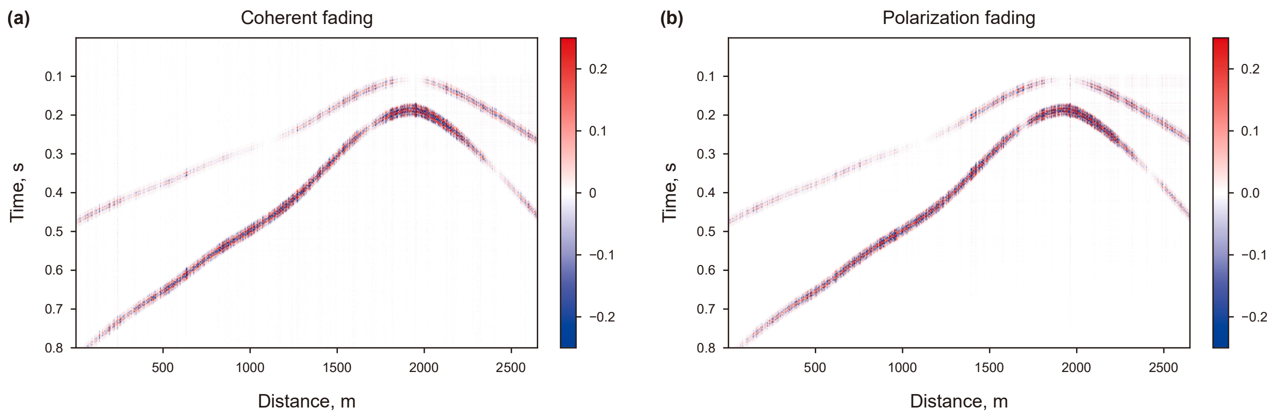

Fig. 8. Comparison of DAS simulations under coherent fading (**a**) and polarization fading (**b**).

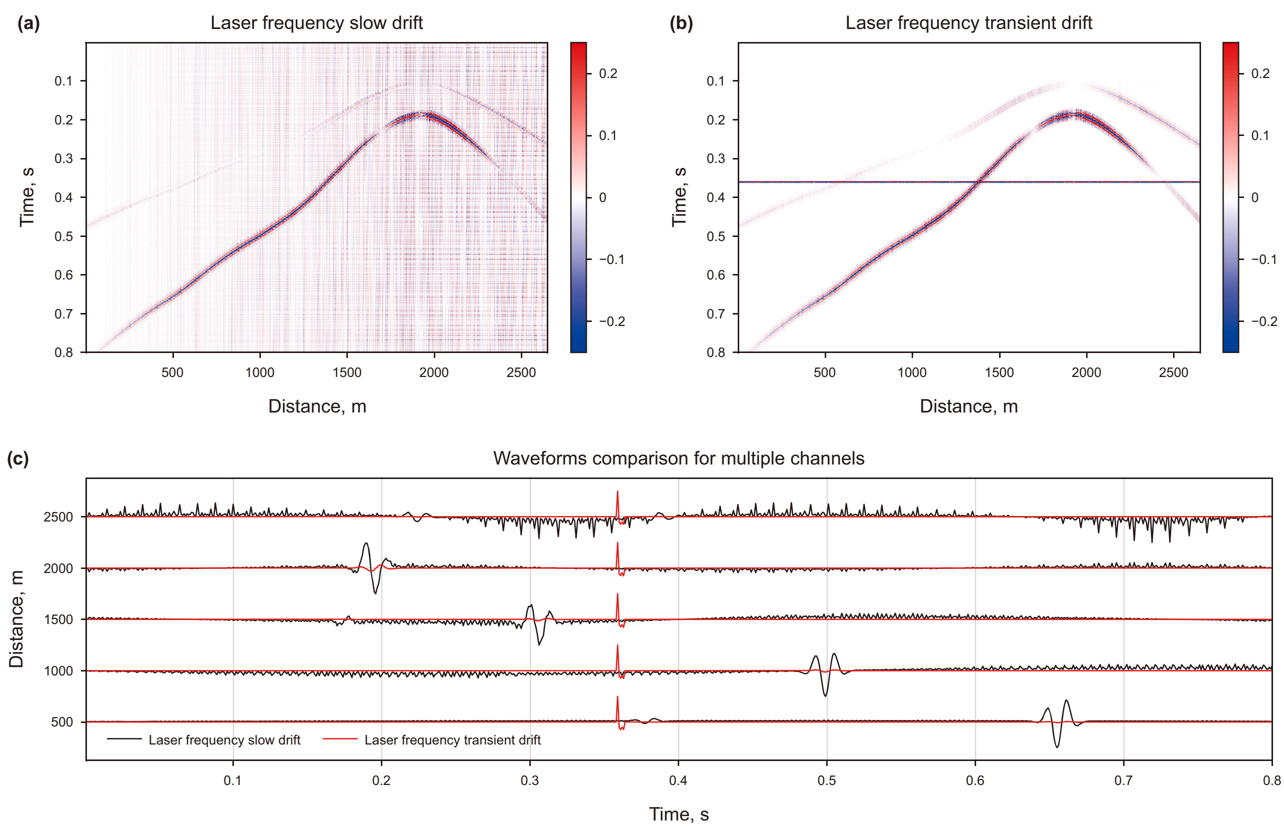

Fig. 9. Effects of laser frequency drift on DAS responses. (**a**) Simulation under continuous slow frequency drift; (**b**) simulation under transient frequency jump; (**c**) comparison of waveforms from multiple channels, with black curves representing slow drift and red curves representing transient drift. It can be seen that in the case of slow drift, the waveforms of vibration signals across channels generally maintain their overall shape, showing only gradual shifts accumulated over time. In contrast, under transient jumps, all channels exhibit simultaneous anomalies in both amplitude and phase at the same moment.

noise or horizontal noise. Common-mode frequency noise may be misinterpreted as a simultaneous vibration event, potentially complicating the interpretation of actual DAS observations. It should be noted that the appearance of such a horizontal line indicates a phase anomaly across all channels. While frequency drift can produce this phenomenon, it is not necessarily the cause; more commonly, it arises from external disturbances.

3.5. DAS responses to instrumental noise

Instrumental noise mainly originates from the balanced photodetector and subsequent electronic circuits, manifesting as broadband random noise. In our simulations, BPD noise was introduced as additional high-frequency background speckle superimposed on the signal. Based on our actual measurement, the instrument noise level is about 1% of the average intensity of the effective signal. Fig. 10 illustrates the DAS responses under typical instrumental noise conditions. It can be observed that the presence of noise introduces uniformly distributed fine speckles in the background of the records, leading to a reduction in the overall SNR compared with the noise-free case. Unlike coherent fading or frequency drift noise, instrumental noise does not produce systematic stripe patterns or global phase shifts in the records; instead, it appears as broadband random perturbations

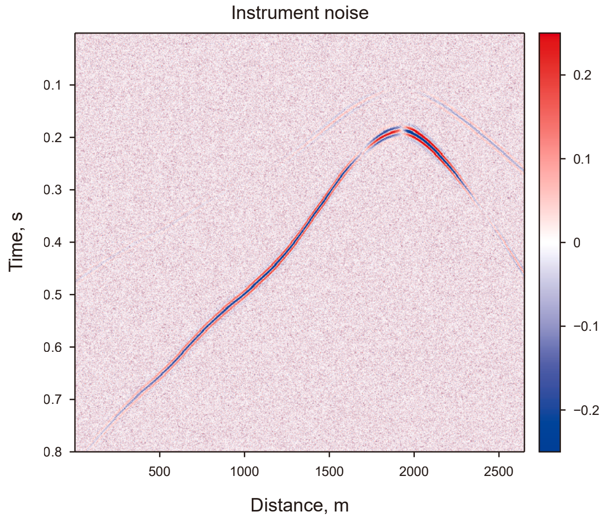

Fig. 10. Effects of instrumental noise on DAS responses.

superimposed on the signal. Its characteristic feature is a relatively uniform effect across the entire record (becoming more pronounced in weak-signal regions), primarily manifested as an elevation of the background noise floor.

3.6. DAS responses to pulse width and gauge length

The laser pulse width and gauge length are critical factors determining the data acquisition quality of DAS systems. To investigate their combined effects, we performed simulations incorporating all relevant parameters, rather than isolating individual factors. Fig. 11(a)–(c) compare DAS responses with a fixed pulse width of 2 m and gauge lengths of 2 m, 4 m, and 8 m, respectively. Several systematic trends can be observed:

1) Improved overall SNR: A longer gauge length is equivalent to applying convolutional smoothing to the axial phase gradient after demodulation, averaging perturbations over a larger spatial region. As a result, random noise is partially suppressed,

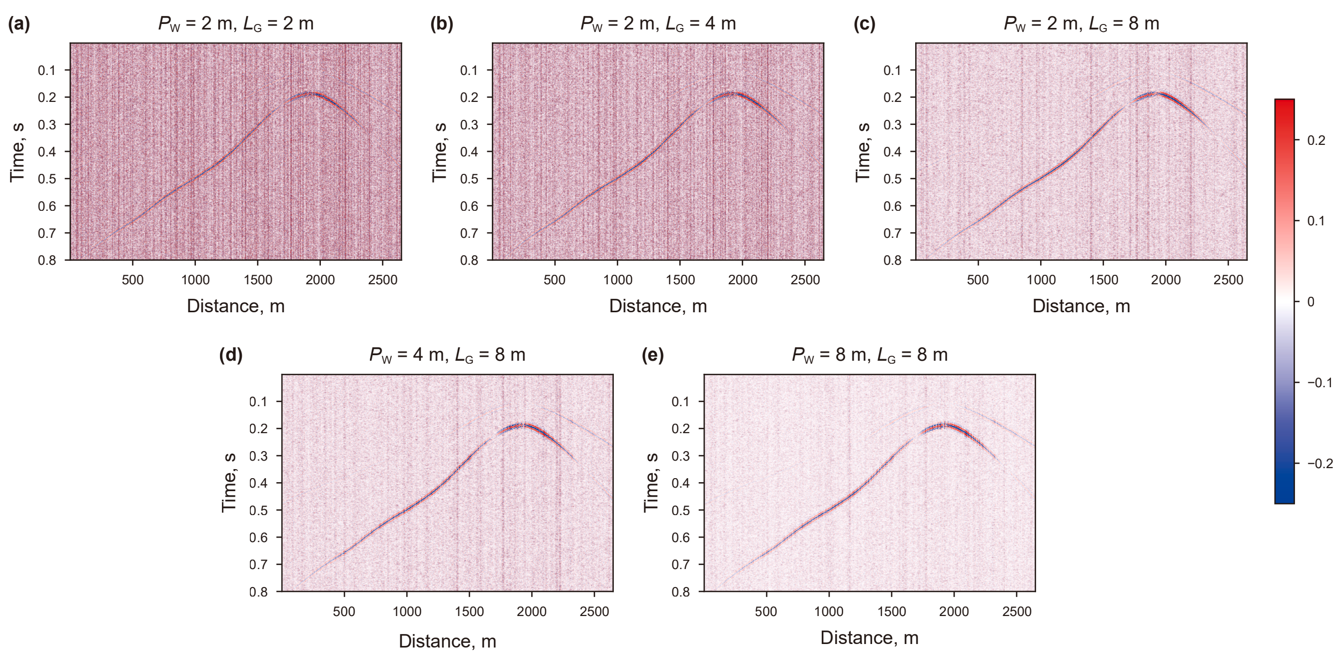

Fig. 11. Influence of gauge length and pulse width on physics-based DAS responses. Top figures show results with a fixed pulse width of 2 m and gauge lengths of **(a)** 2 m, **(b)** 4 m, and **(c)** 8 m, illustrating the trade-off between spatial resolution and signal-to-noise ratio as the gauge length increases. Bottom figures present responses with a fixed gauge length of 8 m and pulse widths of **(d)** 4 m and **(e)** 8 m, highlighting the influence of pulse width on coherent averaging, fading suppression.

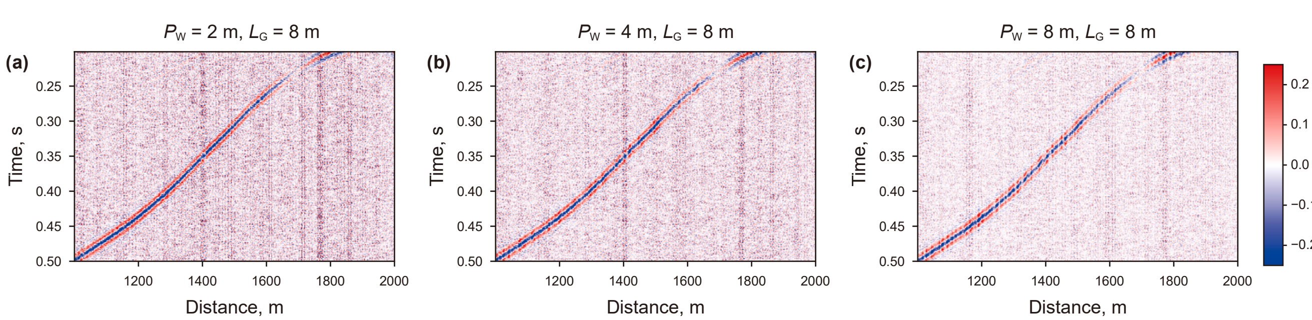

Fig. 12. Zoomed-in comparison of DAS responses illustrating pulse-width-induced distortion under a fixed gauge length. Enlarged views corresponding to Fig. 11(c)–(e), all simulated with a gauge length of 8 m but different pulse widths. Although the nominal gauge length remains unchanged, increasing pulse width leads to progressive waveform distortion and residual fluctuations, indicating an effective loss of spatial resolution caused by excessive pulse overlap.

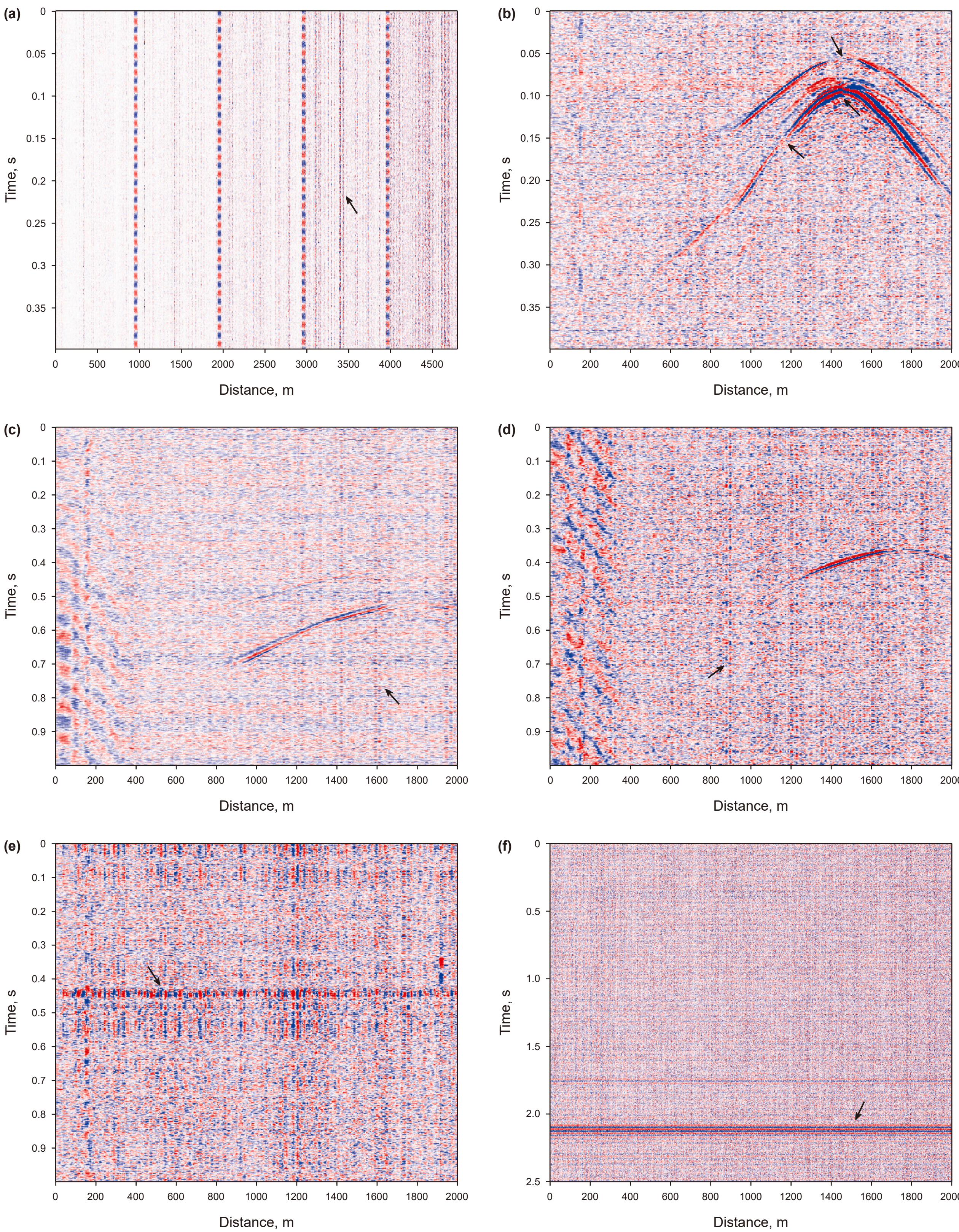

Fig. 13. Representative laboratory and field examples**. (a)** Laboratory experiment with four periodically excited PZTs, shown as four vertical response lines; arrows indicate vertical noise streaks caused by fading effect. **(b)** A recorded microseismic event exhibiting polarity-reversal features consistent with our synthetic modeling results. **(c)–(d)** Examples of vertical noise, **(e)–(f)** field examples of horizontal noise.

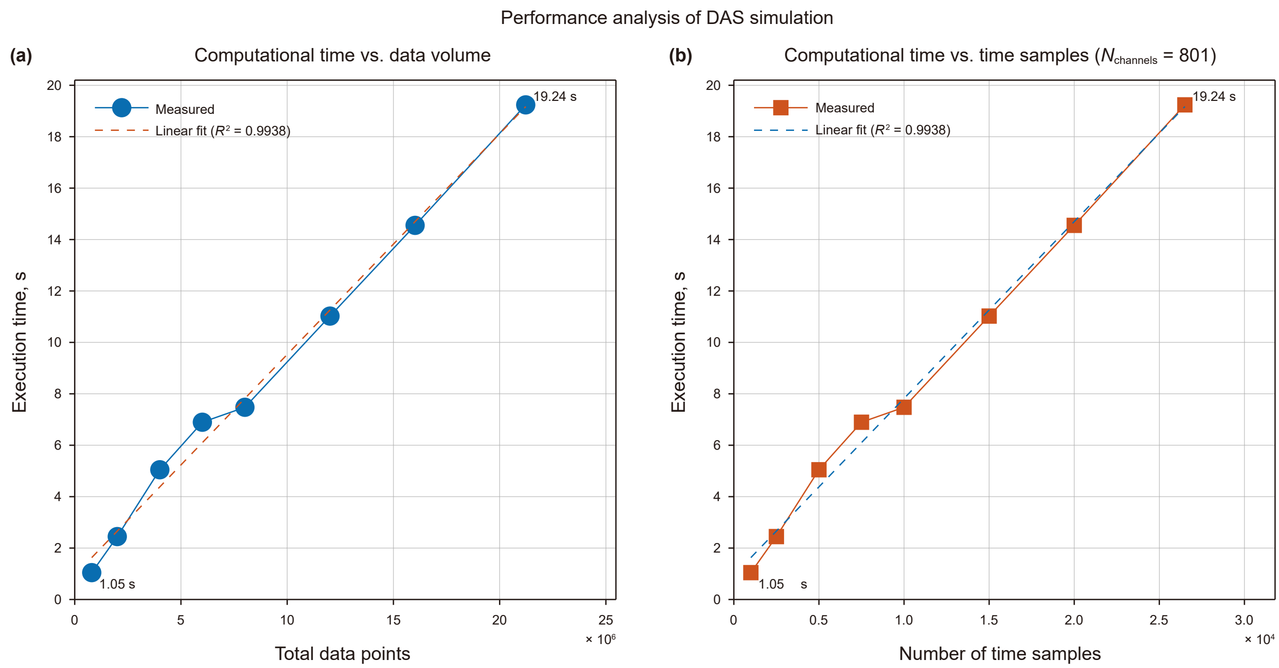

Fig. 14. Computational performance analysis of the DAS simulation method. **(a)** Execution time as a function of total data volume, showing approximately linear scaling behavior with a coefficient of determination $R^2 = 0.9938$. The red dashed line represents the linear fit to the measured data. **(b)** Execution time versus the number of temporal samples for a fixed spatial channel count ($N = 801$).

background speckle diminishes, and waveform amplitudes become clearer.

2) Reduced fading stripe contrast: For short gauge lengths, vertical stripe patterns primarily arise from coherent or polarization fading. As the gauge length increases, the contrast of these stripes decreases significantly, demonstrating the ability of spatial averaging to suppress fading noise and partially mitigate amplitude collapses caused by random constructive/destructive interference.
3) Persistence of residual noise: Although longer gauge lengths improve SNR and suppress fading stripes, they do not fully eliminate noise. When the gauge length increases from 4 m to 8 m, weak residual stripes and fluctuations remain visible in the background. This suggests that simply extending the gauge length cannot completely remove coherent/polarization fading noise, and excessively long gauge lengths reduce spatial resolution, resulting in diminishing returns.

Fig. 11(c)–(e) further compare DAS responses under different pulse widths. As the pulse width increases, the total energy of each pulse grows proportionally with its duration. Although the peak power decreases, the longer pulse duration enhances cumulative Rayleigh backscattering intensity, yielding higher signal amplitudes relative to the detector noise floor. Moreover, wider pulses exert a temporal smoothing effect on random phase fluctuations, reducing depth-dependent fading variations. Consequently, background speckle noise decreases substantially, and fading stripes become elongated and diluted.

However, it should be noted that although a wider pulse improves the signal-to-noise ratio, it inevitably reduces spatial resolution. Fig. 12 presents a zoomed-in view of Fig. 11(c)–(e). Although all three cases share the same gauge length of 8 m, and thus the same nominal spatial resolution, the response with a pulse width of 8 m exhibits more pronounced fluctuations and data distortion. This indicates that an excessively wide pulse leads to an effective loss of spatial resolution in practice.

3.7. Observation of actual DAS data

To further validate the effectiveness of the method, we provide several additional examples, including laboratory experiments. As shown in Fig. 13(a), four vertical lines indicate the locations of four piezoelectric transducers (PZTs), which were driven to vibrate periodically according to a prescribed input signal. Such controlled laboratory experiments represent an essential validation approach for assessing the baseline performance of DAS systems. The arrows highlight the presence of vertical noise streaks caused by coherent fading. Although modern DAS interrogators commonly employ multi-frequency or multi-pulse schemes to mitigate fading, this effect cannot be completely eliminated and remains observable in practice (Fig. 13(c) and (d)).

Fig.13(b) shows a microseismic event whose waveform characteristics closely resemble the synthetic results presented earlier in this study, including the polarity-reversal pattern predicted by our modeling. Fig. 13(e) and (f) present representative examples of horizontal noise in field DAS data, further confirming the prevalence of such optical noise in real observations.

These examples clearly demonstrate that various forms of optical noise are intrinsic to DAS measurements and persist across both laboratory and field environments. Therefore, the numerical simulation framework proposed in this work, which incorporates the full optical demodulation chain, provides a physically realistic means of reproducing these phenomena. By capturing these non-ideal effects, our model offers improved interpretability of DAS observations and enhances the reliability of subsequent data analysis and inversion.

3.8. Computational efficiency

In this section, we will discuss the computational efficiency of the proposed DAS numerical simulation method. But it should be noted that in this simulation framework, our primary focus is on the influence of the optical system on DAS responses. Therefore, we do not account for the time required to compute displacements via numerical methods, whether through analytical solutions, finite-difference, or finite-element approaches. Instead, we are concerned with the time needed to obtain the DAS signals after displacements have been computed, i.e., the time required for optical demodulation.

Fig. 14 presents the computational performance characteristics of the DAS simulation method. The spatial grid consisted of 801 channels, while the temporal sampling points were varied from 1,000 to 26,500 to assess scalability. As shown in Fig. 14(a), the execution time exhibits a nearly linear relationship with the total data volume, with a coefficient of determination (R^2) of 0.9938, indicating excellent predictability of computational cost. For a representative case 801 $\times$ 26,500 grid points (2.12 $\times$ 10^7 data points), the execution time is approximately 19.24 s. Fig. 14(b) illustrates the relationship between computational time and the number of temporal samples for a fixed number of spatial channels ($N = 801$). The average processing rate across all tested configurations is approximately 9.52 $\times$ 10^5 points per second, which translates to efficient handling of realistic DAS monitoring scenarios. For instance, a typical field deployment with 1,000 channels and a 1 kHz sampling rate would generate 10^6 samples per second, which our simulation framework can process in near real-time on standard computational hardware.

In summary, the computational performance analysis demonstrates that the proposed DAS simulation framework achieves excellent scalability with near-linear complexity, making it practical for large-scale seismic monitoring applications.

4. Discussion

The proposed beyond spatial averaging DAS seismic response model incorporates optical processes that are absent in conventional approaches, thereby generating simulations that more closely resemble real systems. The physical implications of the results warrant careful consideration. In the noise-included comparison tests, the physics-based model produced smoother responses than the simplified model, suggesting that the optical detection and demodulation processes in real DAS systems inherently act as filters for high-frequency noise. This finding implies that traditional approaches, which directly superimpose noise onto the wavefield before spatial averaging, may overestimate the impact of noise on DAS data. By incorporating realistic optical processes, the system's intrinsic filtering capability is revealed to buffer part of the noise. This is encouraging for DAS data analysis, as it suggests that real systems may be more robust than idealized models. Nevertheless, it must be emphasized that this result was obtained under idealized conditions. In more complex scenarios, different noise sources may couple with each other, and the actual denoising performance requires further case-specific analysis. Moreover, the differences observed between simplified and physics-based models under noisy conditions underscore the necessity of considering optical processes when studying DAS noise characteristics; otherwise, key details may be overlooked.

The applicability and limitations of the model are also important considerations. This model is applicable to DAS systems based on coherent OTDR, primarily for fibers that are mostly straight or have small-angle bends, and that are tightly coupled with the surrounding medium—for example, downhole fibers in cemented sections or directly buried optical cables. Moreover, the model is more suitable for applications where seismic waves predominantly propagate parallel to the fiber, such as vertical seismic profiling (VSP). Conversely, scenarios in which the model is less suitable include fibers with poor coupling, as well as cases where seismic waves are predominantly incident along the fiber axis. In such cases, the model may predict a near-zero response, while in reality, weak signals may still be recorded due to the Poisson effect. Future improvements of the method should focus on the following aspects: 1) Investigating the transfer of seismic waves from the medium to the fiber, such as slip boundaries at fiber–interface contacts. 2) Incorporating shape sensing and analyzing sensitivity to fiber bending. 3) Introducing semi-empirical correction terms for axial incidence, based on laboratory experiments.

However, the model has significant potential for application in data processing and system optimization. By comparison with field data, it can replicate various optical noise effects, thereby offering a platform for developing noise-resistant signal processing algorithms. Previous artificial intelligence–based denoising approaches typically relied on training with combined field noise and synthetic seismic records (Saad et al., 2024; Gu et al., 2024). In contrast, our approach generates synthetic DAS data directly incorporating optical noise, effectively overcoming this limitation. The simulated results can serve as training datasets for deep learning algorithms, improving their capability to identify and classify complex seismic signals, thereby enhancing DAS monitoring and prediction performance. Moreover, the model can function as a virtual experimental platform to evaluate the influence of fiber length, laser specifications, and detector performance on data quality, supporting system design and optimization.

In summary, the proposed physics-based simulation framework provides a powerful tool for evaluation of DAS system performance and guidance for its application in seismology. However, further improvements are needed, including validation against more field data and the incorporation of more complex simulation scenarios.

5. Conclusions

This study addresses the limitations of current DAS seismic response simulations, which often rely excessively on spatial averaging approximations while neglecting key optical processes. We propose a high-fidelity numerical simulation framework that incorporates optical scattering and coherent demodulation mechanisms. The main conclusions are as follows:

1) A DAS simulation model was established. We combined elastic wavefield simulation with fiber Rayleigh scattering, coherent detection, and signal demodulation, thereby constructing a physical model covering laser emission, fiber scattering, optical interference, and digital demodulation. The model explicitly incorporates key factors such as refractive index perturbations, statistical variations of scattering coefficients, polarization randomness, laser frequency drift, phase noise, and detector noise, making it more consistent with the actual operating mechanisms of DAS systems.
2) Systematic quantification of parameter effects on DAS responses. Through simulation experiments, we analyzed the influence of pulse width, gauge length, polarization state, laser frequency drift, and detector noise on DAS data quality. For instance, increasing pulse width and gauge length improves the

signal-to-noise ratio but reduces spatial resolution; polarization randomness and scattering fluctuations generate fading blind zones; frequency drift must be constrained to avoid common-mode errors; and detector noise determines the detection threshold for weak vibrations. These findings provide practical guidance for optimizing DAS system parameters across different application scenarios.

3) Comparison with field data confirms the model's applicability. The synthetic DAS responses generated by our model were compared with monitoring data from a shale gas hydraulic fracturing site. The model successfully reproduced the main signal and noise characteristics observed in the field, demonstrating its reliability and potential as a tool for interpreting field data and supporting system optimization.

CRediT authorship contribution statement

Yi Yao: Writing – original draft, Validation, Software, Methodology, Investigation, Conceptualization. **Yi-Bo Wang:** Writing – review & editing, Supervision, Methodology, Conceptualization.

Declaration of competing interest

The authors declare that they have no known competing financial interests or personal relationships that could have appeared to influence the work reported in this paper.

Acknowledgment

This work was supported by the National Science Fund for Distinguished Young Scholars (Grant No. 42025403) and the National Natural Science Foundation of China (Grant Nos. 42442403, 42404145).

References

Ajo-Franklin, J.B., Dou, S., Lindsey, N.J., et al., 2019. Distributed acoustic sensing using dark fiber for near-surface characterization and broadband seismic event detection. Sci. Rep. 9, 1–14. https://doi.org/10.1038/s41598-018-36675-8.

Cole, S., Karrenbach, M., 2019. Multi-well DAS observations for hydraulic fracture monitoring. In: Proceedings of the Fifth EAGE Workshop on Borehole Geophysics, EAGE Conference Proceedings. https://doi.org/10.3997/2214-4609.2019X604059.

Eaid, M., 2022. Distributed Acoustic Sensing: Modelling, Full Waveform Inversion, and its Use in Seismic Monitoring. Ph.D. Thesis, University of Calgary, Calgary, Canada.

Grandi, S., Dean, M., Tucker, O., 2017. Efficient containment monitoring with distributed acoustic sensing: Feasibility studies for the former Peterhead CCS project. Energy Proc. 114, 3889–3904. https://doi.org/10.1016/j.egypro.2017.03.152.

Gu, X., Collet, O., Tertyshnikov, K., et al., 2024. Removing instrumental noise in distributed acoustic sensing data: A comparison between two deep learning approaches. Remote Sens. 16, 4150. https://doi.org/10.3390/rs16224150.

Ichikawa, M., Uchida, S., Katou, M., et al., 2020. Case study of hydraulic fracture monitoring using multiwell integrated analysis based on low-frequency DAS data. Lead. Edge 39, 794–800. https://doi.org/10.1190/tle39110794.1.

Jakkampudi, S., Shen, J., Li, W., et al., 2020. Footstep detection in urban seismic data with a convolutional neural network. Lead. Edge 39, 654–660. https://doi.org/10.1190/tle39090654.1.

Jin, G., Friehauf, K., Roy, B., et al., 2019a. Fiber Optic Sensing-based Production Logging Methods for low-rate Oil Producers. In: SPE/AAPG/SEG Unconventional Resources Technology Conference, URTEC-2019-943-MS. https://doi.org/10.15530/urtec-2019-943.

Jin, G., Mendoza, K., Roy, B., Buswell, D.G., 2019b. Machine learning-based fracture-hit detection algorithm using low-frequency DAS signal. Lead. Edge 38, 520–524. https://doi.org/10.1190/tle38070520.1.

Jin, G., Roy, B., 2017. Hydraulic-fracture geometry characterization using low-frequency DAS signal. Lead. Edge 36, 975–980. https://doi.org/10.1190/tle36120975.1.

Kim, J., Johnson, W.B., Kanakaraju, S., et al., 2009. Demonstration of balanced coherent detection using polymer optical waveguide integrated distributed traveling-wave photodetectors. Opt. Express 17, 20242–20248. https://doi.org/10.1364/OE.17.020242.

Kok, S.P., Go, Y.I., Wang, X., et al., 2024. Advances in fiber Bragg grating sensing: A review of conventional and new approaches and novel sensing materials in harsh and emerging industrial sensing. IEEE Sens. J. 24 (19), 29485–29505. https://doi.org/10.1109/JSEN.2024.3434351.

Lecoulant, J., Ma, Y., Dettmer, J., Eaton, D.W., 2023. Strain-based forward modeling and inversion of seismic moment tensors using distributed acoustic sensing observations. Front. Earth Sci. 11, 1176921. https://doi.org/10.3389/feart.2023.1176921.

Lellouch, A., Biondi, B.L., Yuan, S., 2021. Seismic applications of downhole distributed acoustic sensing. Sensors 21, 2897. https://doi.org/10.3390/s21092897.

Lellouch, A., Yuan, S., Ellsworth, W.L., et al., 2020. Comparison between distributed acoustic sensing and geophones: Downhole microseismic monitoring of the FORGE geothermal experiment. Seismol Res. Lett. 91, 3256–3268. https://doi.org/10.1785/0220200149.

Li, C., Liu, Z., Zhuang, Y., et al., 2023. Phase-correction-based SNR enhancement for distributed acoustic sensing with strong environmental background interference. Opt Laser. Eng. 168, 107678. https://doi.org/10.1016/j.optlaseng.2023.107678.

Lindsey, N.J., Rademacher, H., Ajo-Franklin, J.B., 2020. On the broadband instrument response of fiber-optic DAS arrays. J. Geophys. Res. Solid Earth 125. https://doi.org/10.1029/2019JB018145 e2019JB018145.

Liokumovich, L.B., Ushakov, N.A., Kotov, O.I., et al., 2015. Fundamentals of optical fiber sensing schemes based on coherent optical time domain reflectometry: Signal model under static fiber conditions. J. Lightwave Technol. 33, 3660–3671.

Lior, I., Sladen, A., Rivet, D., et al., 2021. On the detection capabilities of underwater distributed acoustic sensing. J. Geophys. Res. Solid Earth 126. https://doi.org/10.1029/2020JB020925 e2020JB020925.

Liu, F., Xie, S.R., Zhang, M., et al., 2020. Downhole microseismic monitoring using time-division multiplexed fiber-optic accelerometer array. IEEE Access 8, 120104–120113. https://doi.org/10.1109/ACCESS.2020.3003374.

Lu, Y.L., Zhu, T., Chen, L., Bao, X., 2010. Distributed vibration sensor based on coherent detection of phase-OTDR. J. Lightwave Technol. 28, 3243–3249.

Masoudi, A., Newson, T.P., 2017. Analysis of distributed optical fibre acoustic sensors through numerical modelling. Opt. Express 25, 32021–32040. https://doi.org/10.1364/OE.25.032021.

Mateeva, A., Lopez, J., Potters, H., et al., 2014. Distributed acoustic sensing for reservoir monitoring with vertical seismic profiling. Geophys. Prospect. 62, 679–692. https://doi.org/10.1111/1365-2478.12116.

Matsumoto, H., Araki, E., Kimura, T., et al., 2021. Detection of hydroacoustic signals on a fiber-optic submarine cable. Sci. Rep. 11, 2797. https://doi.org/10.1038/s41598-021-82093-8.

Molteni, D., Williams, M.J., Wilson, C., 2017. Detecting microseismicity using distributed vibration sensing. First Break 35, 51–55. https://doi.org/10.3997/1365-2397.35.4.87841.

Nishimura, T., Emoto, K., Nakahara, H., et al., 2021. Source location of volcanic earthquakes and subsurface characterization using fiber-optic cable and distributed acoustic sensing system. Sci. Rep. 11, 6319. https://doi.org/10.1038/s41598-021-85621-8.

Ren, M., Lu, P., Chen, L., Bao, X., 2016. Theoretical and experimental analysis of φ-OTDR based on polarization diversity detection. IEEE Photon. Technol. Lett. 28, 697–700. https://doi.org/10.1109/LPT.2015.2504968.

Saad, O.M., Ravasi, M., Alkhalifah, T., 2024. Noise attenuation in distributed acoustic sensing data using a guided unsupervised deep learning network. Geophysics 89, V573–V587. https://doi.org/10.1190/geo2024-0109.1.

Sha, Z., Feng, H., Zeng, Z., 2017. Phase demodulation method in phase-sensitive OTDR without coherent detection. Opt. Express 25, 4831–4844. https://doi.org/10.1364/OE.25.004831.

Shearer, P.M., 2009. In: Introduction to Seismology, second ed. Cambridge University Press, Cambridge, UK.

Spikes, K.T., Tisato, N., Hess, T.E., Holt, J.W., 2019. Comparison of geophone and surface-deployed distributed acoustic sensing seismic data. Geophysics 84, A25–A29. https://doi.org/10.1190/geo2018-0528.1.

Vera Rodriguez, I., Wuestefeld, A., 2020. Strain microseismics: Radiation patterns, synthetics, and moment tensor resolvability with distributed acoustic sensing in isotropic media. Geophysics 85, KS101–KS117. https://doi.org/10.1190/geo2019-0373.1.

Walter, F., Gräff, D., Lindner, F., et al., 2020. Distributed acoustic sensing of microseismic sources and wave propagation in glaciated terrain. Nat. Commun. 11, 2436. https://doi.org/10.1038/s41467-020-15824-6.

Wang, W.J., Chen, L., Wang, Y.B., Peng, F., 2022a. Fiber-optic vibration sensing I: Rotation measurement technique and its seismological applications. Rev. Geophys.Plan. Phys. 53 (1), 1–16. https://doi.org/10.19975/j.dqyxx.2021-046.

Wang, W.J., Chen, L., Wang, Y.B., Peng, F., 2022b. Fiber-optic vibration sensing II: Intrinsic sensing with scattered or transmitted light and their seismological applications. Rev. Geophys.Plan. Phys. 53 (2), 119–137. https://doi.org/10.19975/j.dqyxx.2021-048.

Yao, Y., Wang, Y.B., Wang, W.J., Chen, L., 2023. Micro-vibration response characteristics of distributed acoustic sensing. Chin. J. Geophys. 66, 713–730. https://doi.org/10.6038/cjg2022P0841.

Zhang, L., Chen, L., Bao, X., 2020. Unveiling delay-time-resolved phase noise statistics of narrow-linewidth laser via coherent optical time domain reflectometry. Opt. Express 28, 6719–6733. https://doi.org/10.1364/OE.387185.

Zhang, L.L., Zhao, Y., Liu, L., et al., 2024. Far-field radiation patterns of distributed acoustic sensing in anisotropic media with an explosive source and vertically straight fiber. Pet. Sci. 22 (2), 641–652. https://doi.org/10.1016/j.petsci.2024.10.003.

Zhao, L., Zhang, X., Xu, Z., 2024. A high-fidelity numerical model of coherent φ-OTDR. Measurement 230, 114526. https://doi.org/10.1016/j.measurement.2024.114526.

Zhong, Z., Zou, N., Zhang, X., 2021. Accurate measurement for the subsequent perturbation in the coherent φ-OTDR system with small laser-frequency drift. J. Lightwave Technol. 39, 5973–5979. https://doi.org/10.1109/JLT.2021.3094088.